

Investigation of the optoelectronic properties of a novel polypyrrole-multi-well carbon nanotubes/titanium oxide/aluminum oxide/p-silicon heterojunction

Ashery, Adel; Gaballah, Ahmed E. H.; Elmoghazy, Essam; Basyooni-M.Kabatas, Mohamed A.

DO

10.1515/ntrev-2025-0174

Publication date

Document VersionFinal published version

Published in
Nanotechnology Reviews

Citation (APA)

Ashery, A., Gaballah, A. E. H., Elmoghazy, E., & Basyooni-M.Kabatas, M. A. (2025). Investigation of the optoelectronic properties of a novel polypyrrole-multi-well carbon nanotubes/titanium oxide/aluminum oxide/p-silicon heterojunction. *Nanotechnology Reviews*, *14*(1), Article 20250174. https://doi.org/10.1515/ntrev-2025-0174

Important note

To cite this publication, please use the final published version (if applicable). Please check the document version above.

Copyright

Other than for strictly personal use, it is not permitted to download, forward or distribute the text or part of it, without the consent of the author(s) and/or copyright holder(s), unless the work is under an open content license such as Creative Commons.

Takedown policy

Please contact us and provide details if you believe this document breaches copyrights. We will remove access to the work immediately and investigate your claim.

Research Article

Adel Ashery, Ahmed E. H. Gaballah, Essam Elmoghazy, and Mohamed A. Basyooni-M. Kabatas*

Investigation of the optoelectronic properties of a novel polypyrrole-multi-well carbon nanotubes/titanium oxide/aluminum oxide/ p-silicon heterojunction

https://doi.org/10.1515/ntrev-2025-0174 received January 10, 2025; accepted April 30, 2025

Abstract: The novel design of gold/polypyrrole-multi-walled carbon nanotubes/titanium dioxide/aluminum oxide/P-type silicon/aluminum (Au/PPy-MWCNTs/TiO2/Al2O3/p-Si/Al) is utilized to fabricate supercapacitors, sensors, diodes, and microelectronic devices. The electrical characteristics of the structure are examined both in the dark and under illumination to evaluate its photosensing performance. The real part of the AC conductivity at all voltages and temperatures is observed to be low at low- and mid-frequencies but significantly increases at high frequencies. The imaginary part of the AC conductivity exhibits three distinct behaviors: it is positive at low frequencies and shows both negative and positive values at high frequencies. At specific temperatures, such as 293, 273, and 253 K, the imaginary component of the AC conductivity ($\sigma_{ac''}$) is negative only at high frequencies. In the Cole-Cole diagrams, the symmetrical semicircles increase with temperature for all voltages, except at V = -2 V. The real part of the electric modulus (M) shows positive and negative values; however, at certain temperatures, it is positive. The imaginary part of the modulus (M'') is consistently positive.

Keywords: polypyrrole, multi-walled carbon nanotubes, *I–V* characteristic

Adel Ashery: Solid State Physics Department, Physics Research Institute, National Research Centre, 33 El-Bohouth St, Dokki, Giza, 12622, Egypt **Ahmed E. H. Gaballah, Essam Elmoghazy:** Photometry and Radiometry Division, National Institute of Standards (NIS), Tersa St, Al-Haram, 12211, Giza, Egypt

1 Introduction

Polymer nanocomposites represent an emerging class of materials known for their tunable mechanical, chemical, physical, electrical, and optical properties [1-5]. These properties can be tailored by incorporating different types of nanofillers into polymer matrices and blends [1,6-9]. Environmental polymers are preferable for composite manufacturing because they have a lower negative environmental impact [6]. These polymer nanocomposites are applied as multifunctional material in various applications, such as microelectronics devices, drug distribution, bio-medical, food wrapping, textiles, etc. [8]. Among insulating polymers, the combination of sodium carboxymethyl cellulose (CMC) and polyvinyl alcohol (PVA) plays a crucial role in the synthesis of nanocomposite layers due to their biocompatibility, excellent film-forming ability, ease of synthesis, low-cost, and strong mechanical stability [10,11], miscibility with nanofillers, CMC and PVA create widespread claim as bio-sensors, nanofiltration membrane [11-13], electromagnetic interference (EMI) defensive materials, and also applied in the area of drug distribution, bio-medical [14], and food wrapping [15]. Polypyrrole (PPy) is considered a conductive polymer that has been widely applied owing to its ease of preparation, low cost, ecological and thermal steadiness, great catalytic action, electrical properties, and outstanding optical properties [16-19]. The insufficient mechanical force of PPy bounds its usability, which can be overcome by mixing it with additional isolating polymers to improve mechanical constancy [20]. The presence of PPy in PVA-CMC medium consequences in adapting electrical properties and supporting the mechanical constancy of PPy. Multi-walled carbon nanotube (MWCNT)-based polymer nanocomposites have attracted significant academic and industrial interest due to their promising applications in areas such as charge storage, drug delivery, EMI shielding, supercapacitors, electronic devices, and gas sensors [1–5]. This article presents a novel

^{*} Corresponding author: Mohamed A. Basyooni-M. Kabatas,

Department of Precision and Microsystems Engineering, Delft University of Technology, Mekelweg 2, 2628 CD, Delft, Netherlands; Department of Nanotechnology and Advanced Materials, Graduate School of Applied and Natural Science, Selçuk University, Konya, 42030, Turkey; Solar Research Laboratory, Solar and Space Research Department, National Research Institute of Astronomy and Geophysics, Cairo, Egypt, e-mail: m.kabatas@tudelft.nl, m.a.basyooni@gmail.com

structure, Au/PPy-MWCNTs/TiO₂/Al₂O₃/p-Si/Al, used to produce supercapacitors, diodes, sensors, and microelectronic devices. The synthesis and investigation of its electrical properties were carried out. The real part of the AC conductivity at all voltages and temperatures appeared in the low- and midfrequency ranges, but it significantly increased at high frequencies. The imaginary part of the AC conductivity exhibited three distinct behaviors: at low frequencies, its values were positive, while at high frequencies, it showed both negative and positive values. The third behavior occurred at specific temperatures (293, 273, and 253 K), where σ'_{ac} had only negative values at high frequencies. The real part of the impedance (Z') increased with rising temperature, reaching its maximum at 0 V, but decreased as voltages increased in both the positive and negative regions. The imaginary part of the impedance (Z'') showed peaks with positive values at low frequencies, while at high frequencies, Z" also produced peaks with negative values. In the Cole-Cole diagrams, the semicircles were highly symmetrical and grew with increasing temperature at all voltages, except at V = -2V. The real part of the electric modulus (M) exhibited positive and negative values; however, at specific temperatures like 253, 273, and 293 K, M' had only positive values. The imaginary part of the modulus (M'') consistently showed positive values. The conduction mechanism of the Au/PPy-MWCNTs/TiO₂/ A₁₂O₃/p-Si/Al structure was investigated.

2 Results and discussion

2.1 Experimental procedure

To prepare the Au/PPy-MWCNTs/ $TiO_2/Al_2O_3/n$ -Si/Al structure, a 90:10 weight ratio of PPy and multi-walled carbon nanotubes (MWCNTs) was used created using, with both materials purchased from Sigma Aldrich at a purity level of 99.9%. The process began by depositing a thin film of

aluminum oxide (Al₂O₃) on the surface of a silicon wafer. This was done using a spin coating method, where drops of an Al₂O₃ suspension in water were spread evenly across the surface by rotating the wafer at high speed. Next, a layer of titanium dioxide (TiO₂) was added on top of the Al₂O₃ using the same technique. After the oxide layers were in place, the prepared PPy-MWCNTs composite was applied on top of the TiO₂ layer by drop-casting. This resulted in the final layered structure of PPy-MWCNTs/TiO₂/Al₂O₃. For electrical measurements, gold and aluminum electrodes were deposited on the top and bottom surfaces, respectively.

The surface morphology of the prepared films was examined using a scanning electron microscope. Figure 1(a) shows the MWCNTs with their typical tubular structure, having diameters around 15 nm. In Figure 1(b), after coating with PPy, the nanotubes appear slightly thicker, but their overall fibrous structure remains intact. These images confirm the successful incorporation of the PPy layer onto the nanotubes.

X-ray diffraction analysis, shown in Figure 2, was performed to study the crystal structure of the composite. A strong peak observed at 2θ = 25.3° corresponds to both PPy and MWCNTs, while the peak at 43.7° is attributed specifically to MWCNTs. Additional peaks at 48.1° and 58.46° are associated with the TiO₂ layer. The presence of Al₂O₃ is indicated by a peak at 26.5°, and a peak at 37.8° reflects contributions from both TiO₂ and Al₂O₃. These results confirm the successful deposition and structure of the multi-layered composite film.

Figure 3(a)–(j) displays $\ln f$ dependence of real and imaginary parts of ac conductivity σ_{ac} , σ_{ac} at different temperatures and voltages of Au/PPy-MWCNTs/TiO₂/Al₂O₃/p-Si/Al. In all Figures of σ_{ac} , the curves for all temperatures converge and remain constant without variation across low and mid frequencies. However, at high frequencies, σ_{ac} increases significantly, with the curves at the lowest (223 K) and highest (323 K) temperatures showing a more pronounced rise than the others. For σ_{ac} , the values exhibit dispersion at low frequencies for each

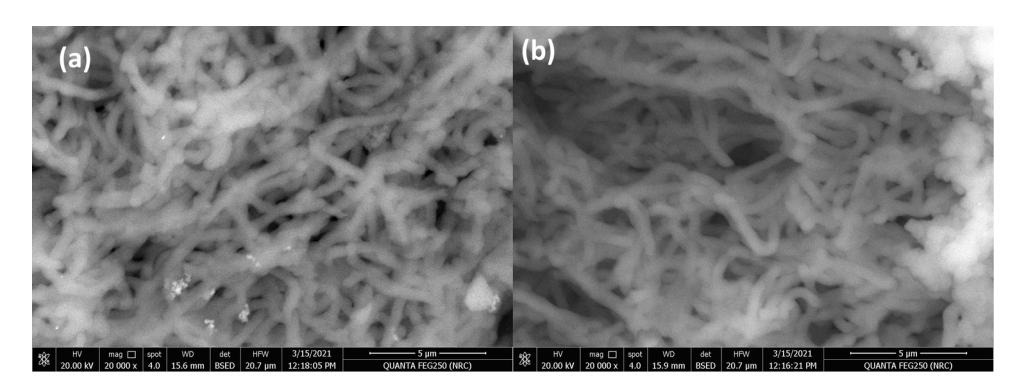


Figure 1: (a) Surface morphology of pristine MWCNTs; (b) MWCNTs coated with PPy.

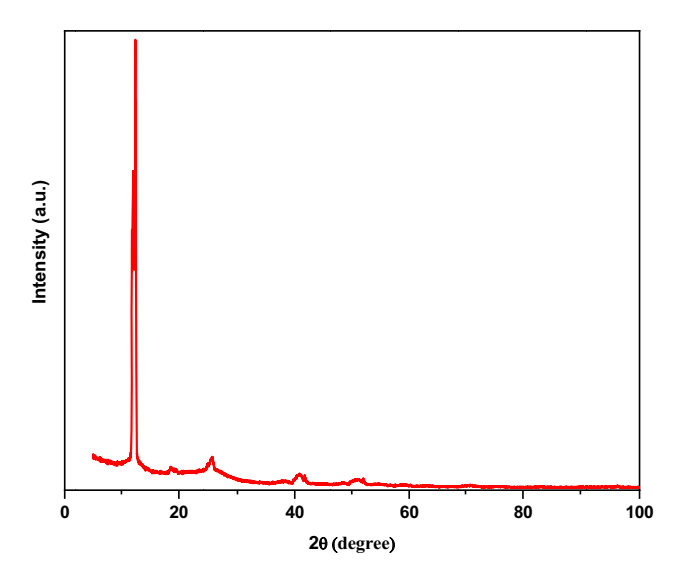


Figure 2: X-ray diffraction pattern of PPy-MWCNTs/TiO₂/Al₂O₃/p-Si.

temperature, with higher values observed at lower temperatures. These values eventually merge, becoming constant across low and mid frequencies. At high frequencies, however, σ''_{ac} displays both negative and positive values. Like σ'_{ac} , σ''_{ac} shows a marked increase at the lowest and highest temperatures compared to the other curves. The nearly linear dependence of σ_{ac} on ln(f), as shown in figures, indicates that the AC conductivity follows a power law, commonly referred to as the "universal dielectric response" [21], as given in the following equations:

$$\sigma_{\rm ac} = \varepsilon'' \omega \varepsilon_0,$$
 (1)

$$\sigma_{ac}(\omega) = \sigma(0) + A\omega^{s}$$
. (2)

Figure 4(a)–(d) illustrates the dependence of $\ln \sigma_{ac}$ with lnf at different temperatures and voltages. In contrast, Figure 2(e)–(h) shows the temperature dependence of the exponent n at voltages (2, -2, 1 and -1 V) for the Au/PPy-MWCNTs/TiO₂/Al₂O₃/p-Si/Al structure. As shown in Figure 2(a)-(d), the AC conductivity exhibits merging and dispersion at low frequencies for each temperature, with its values increasing as the temperature decreases. An exception is observed at a V = -2 V voltage, as shown in Figure 4(a). At high frequencies, σ_{ac} increases linearly, accompanied by a rise in eddy currents [22-24]. This frequencydependent behavior can be described using the power law, as represented by equation (2). Conversely, Figure 4(e)-(h) shows the temperature dependence of the exponent at voltages (2, -2, 1 and -1 V) for the Au/PPy-MWCNTs/ TiO₂/Al₂O₃/p-Si/Al structure. As shown in Figure 4(e) and (g), the exponent increases with rising temperature at 2 and 1 V voltages, whereas in Figure 4(f) and (h), it decreases with increasing temperature at -1 and -2 V voltages. The values

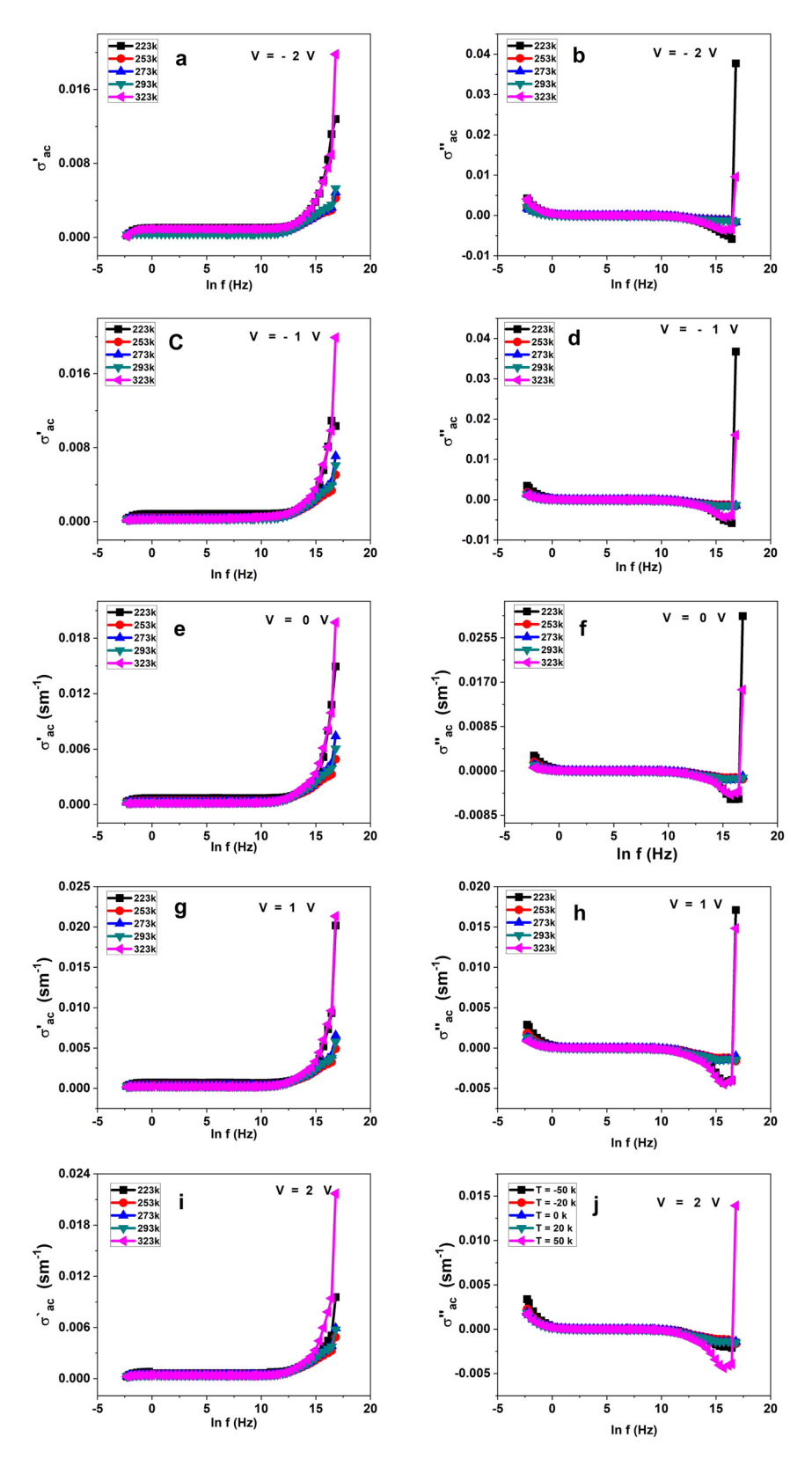
of the exponent range from 0.045 to 0.58, as observed in Figure 2(e)-(h). Additionally, the exponent decreases with temperature at voltages of -1 and -2 V, while it increases with temperature at voltages of 1 and 2V. Therefore, the correlated barrier hopping model, related to the non-intimate valence change pairs, is more suitable to describe the conduction mechanism in these examined nano-crystalline alloys. The AC conductivity and the hopping process of charge carriers can be associated with the density of localized states (EF) [25].

Figure 5(a)–(i) illustrates the frequency dependence of the real (σ_{ac}) and imaginary (σ_{ac}) parts of the ac conductivity at various voltages and temperatures for Au/PPy-MWCNTs/TiO₂/Al₂O₃/p-Si/Al. As shown in Figure 5(a)–(e), the real part of ac conductivity (σ'_{ac}) for all voltages converges and becomes frequency-independent up to lnf = 15. At frequencies higher than $\ln f = 15$, σ_{ac} increases significantly. The imaginary part of impedance (σ''_{ac}) at low frequencies shows positive values for each voltage and then becomes constant. At the same time, peaks with both positive and negative values are observed at high frequencies. as depicted in Figure 3b at 323 K. In Figure 5(d), (f) and (h), $\sigma^{\prime\prime}_{ac}$ behaves similarly, showing only negative values at high frequencies. In Figure 5j, σ'_{ac} follows the same trend as in Figure 3b, with both positive and negative values at high frequencies. The influence of voltage and temperature on AC conductivity is explained by the mobility of charge carriers responsible for hopping. As the temperature increases, the mobility of the hopping ions also rises, thereby enhancing the AC conductivity of the synthesized samples [26].

Figure 6(a)-(j) displays frequency dependence of real and imaginary parts of impedance Z', Z" at different voltages and temperatures of Au/PPy-MWCNTs/TiO₂/Al₂O₃/ p-Si/Al, which is described in as follows:

$$Z^* = Z'(\omega) + Z''(\omega). \tag{3}$$

As shown in Figure 6(a)–(e), the Z' curves at all temperatures and voltages increase with rising temperatures, except at V = -2 V, where plateaus are observed at low and mid frequencies. At high frequencies, the curves decline and converge, reaching a maximum at 0 V and decreasing as the positive or negative voltage increases. Similarly, as depicted in Figure 6(b), (d), (f), (h), and (j), the Z" values increase with temperature, forming positive peaks at low frequencies. However, at mid frequencies, Z" exhibits negative values, forming peaks that grow with temperature. At high frequencies, all curves converge, reaching a minimum. The maximum values of Z" occur at 0 V and decrease with increasing positive and negative voltages. The higher Z' values at low frequencies are attributed to



 $\textbf{Figure 3: (a)-(j)} \ \, \text{In} \textit{f} \textit{vs} \ \, \sigma_{\text{ac'}}, \, \sigma_{\text{ac''}} \ \, \text{at different temperatures and voltages of Au/PPy-MWCNTs/TiO}_2/\text{Al}_2\text{O}_3/\text{p-Si/Al}.$

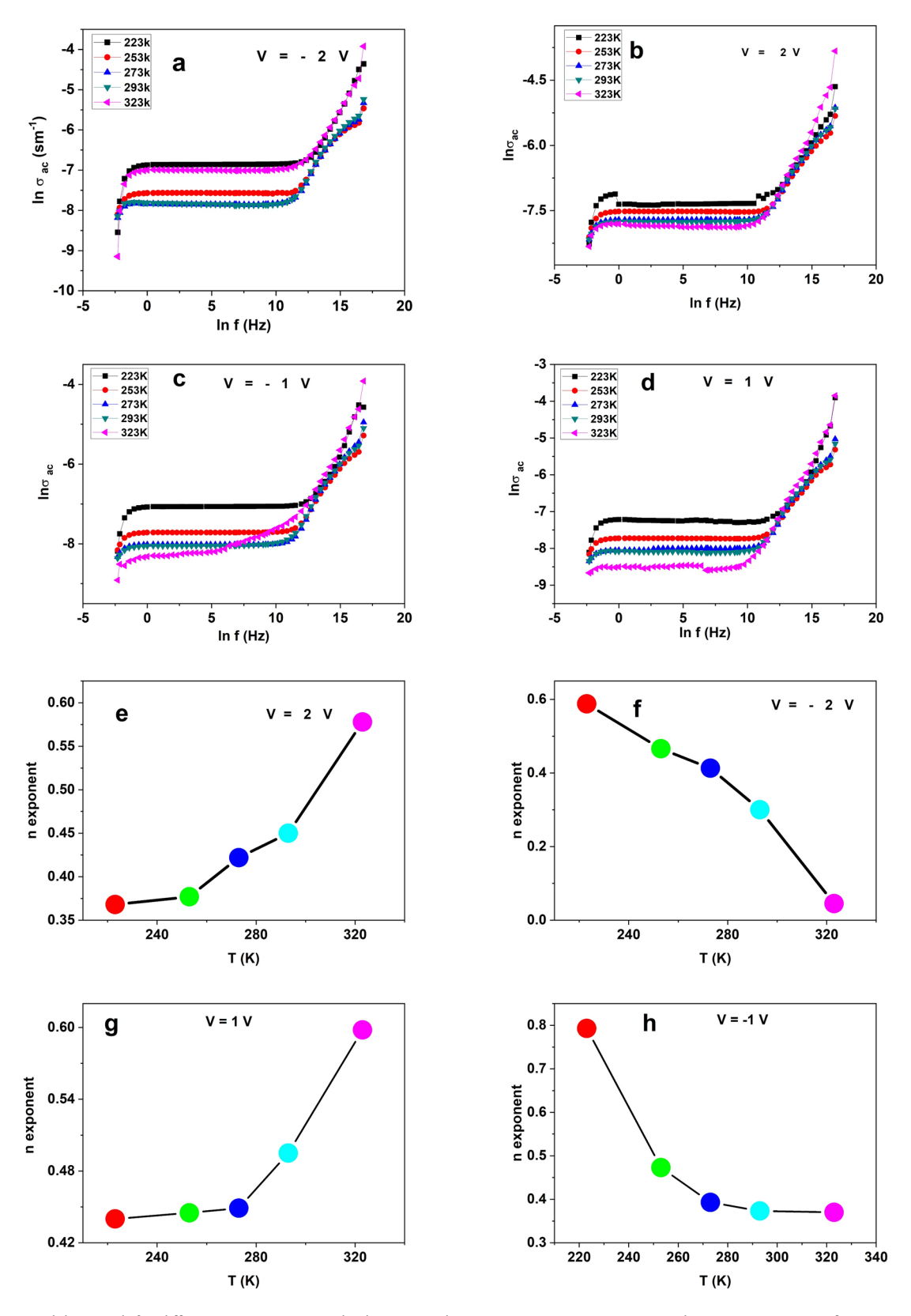
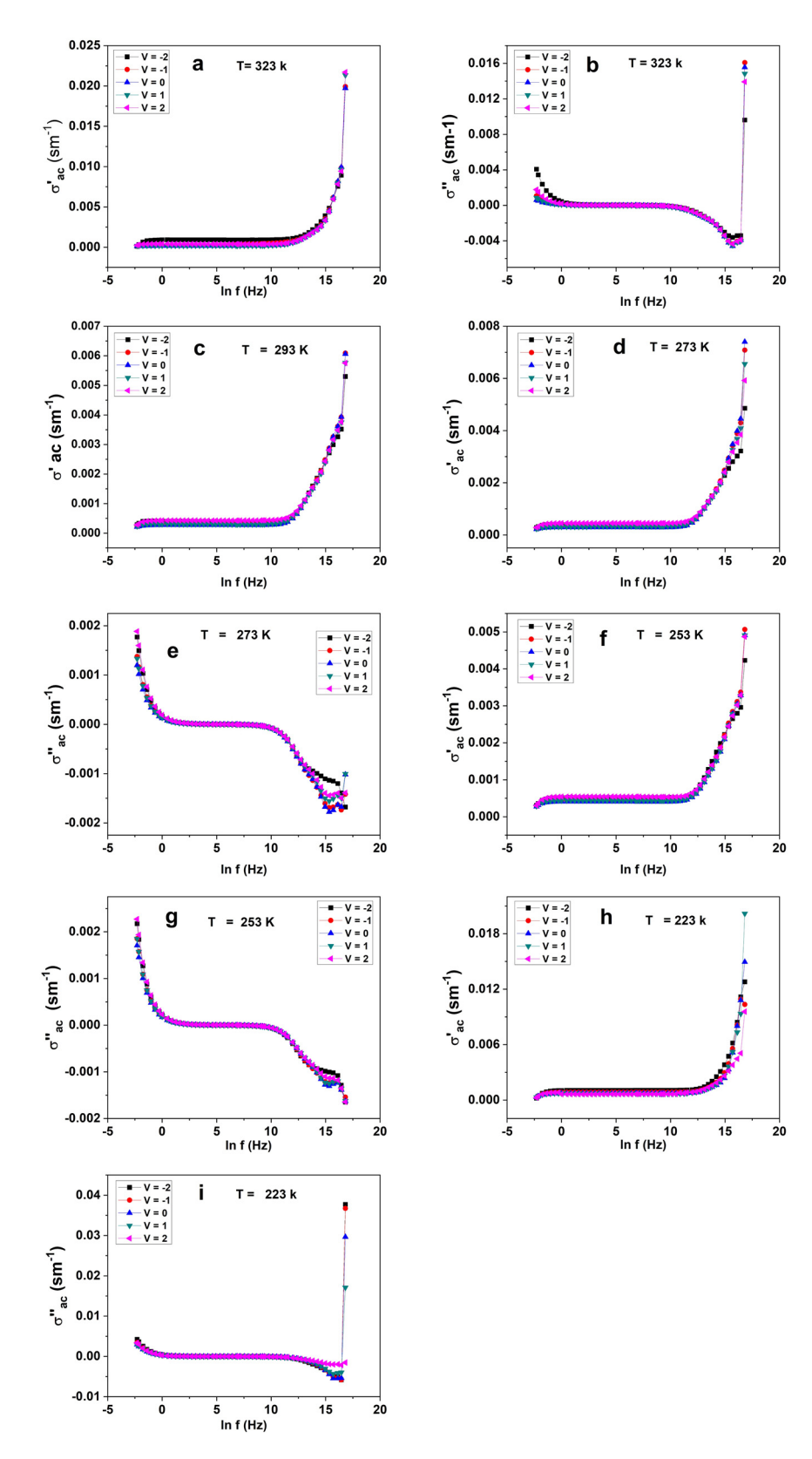


Figure 4: (a)–(d) In σ_{ac} vs Inf at different temperatures and voltages, (e)–(h) n exponent vs temperature at voltages (2, –2, 1, –1 V) of Au/PPy-MWCNTs/ $TiO_2/Al_2O_3/p-Si/Al$.



 $\textbf{Figure 5: (a)-(i) Frequency dependence of } \sigma_{ac}, \sigma_{ac}" \text{ at different voltages and temperatures of Au/PPy-MWCNTs/TiO}_2/Al_2O_3/p-Si/Al.$

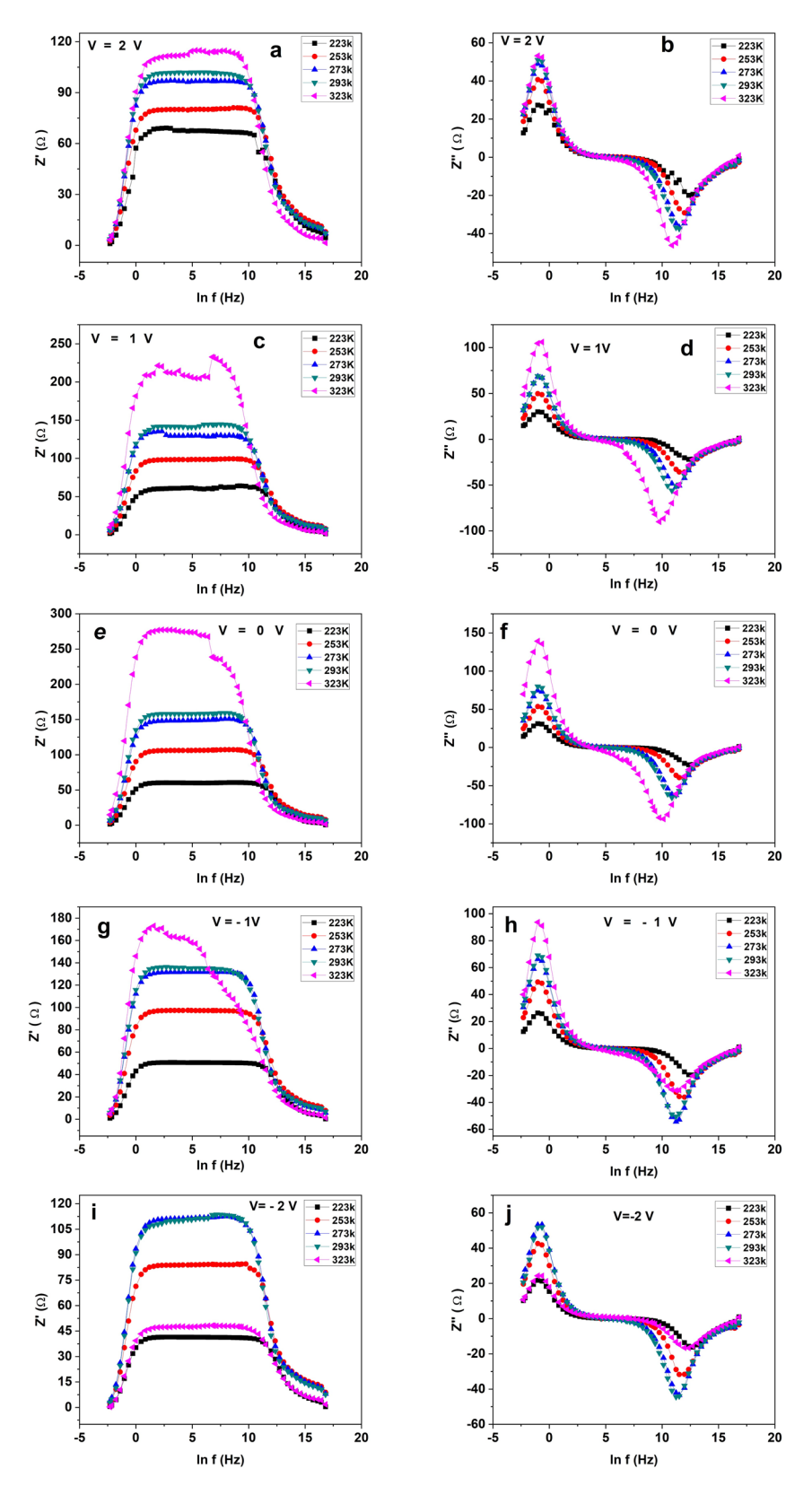


Figure 6: (a)–(j) Frequency dependence of Z', Z" at different voltages and temperatures of Au/PPy-MWCNTs/TiO₂/Al₂O₃/p-Si/Al.

pronounced structural effects, such as surface morphology, grain boundaries, pores, and space charge polarity. The reduction in Z' with increasing frequency in the samples indicates a potential enhancement in AC conductivity [27]. At high frequencies, the Z' plateau of all samples converging at all temperatures suggests the potential for free movement of space charge polarity within the samples, reducing the barrier width [28]. Henceforth, the electrical conductivity increases with a temperature rise and relies on freedom of space charge polarity [29].

Figure 7(a)–(e) shows the Col–Col diagram of Z'' versus Z' at different temperatures and voltages for Au/PPy-MWCNTs/TiO₂/Al₂O₃/p-Si/Al. As depicted in all figures, the Col–Col diagrams at all temperatures and voltages exhibit

ideal and complete semicircles. The radius of the semicircles increases with temperature, except at V=-2V, where the semicircles increase with temperature in the order 223, 323, 253, 293, and 273 K. All semicircles show positive and negative values, with the maximum radius occurring at V=0 V, after which it decreases with increasing positive and negative voltages. The performance of the heterostructures was correlated with an equivalent electrical circuit model, consisting of the parallel assembly of a constant phase element and resistance $(R_{\rm p})$ in series with $R_{\rm s}$ [30–32]. An appropriate equivalent electrical circuit for the heterostructures is presented in Figure 5f. The $R_{\rm s}$ in the heterostructures are attributed to the resistance within the active layer and the ohmic contact of the fabricated device

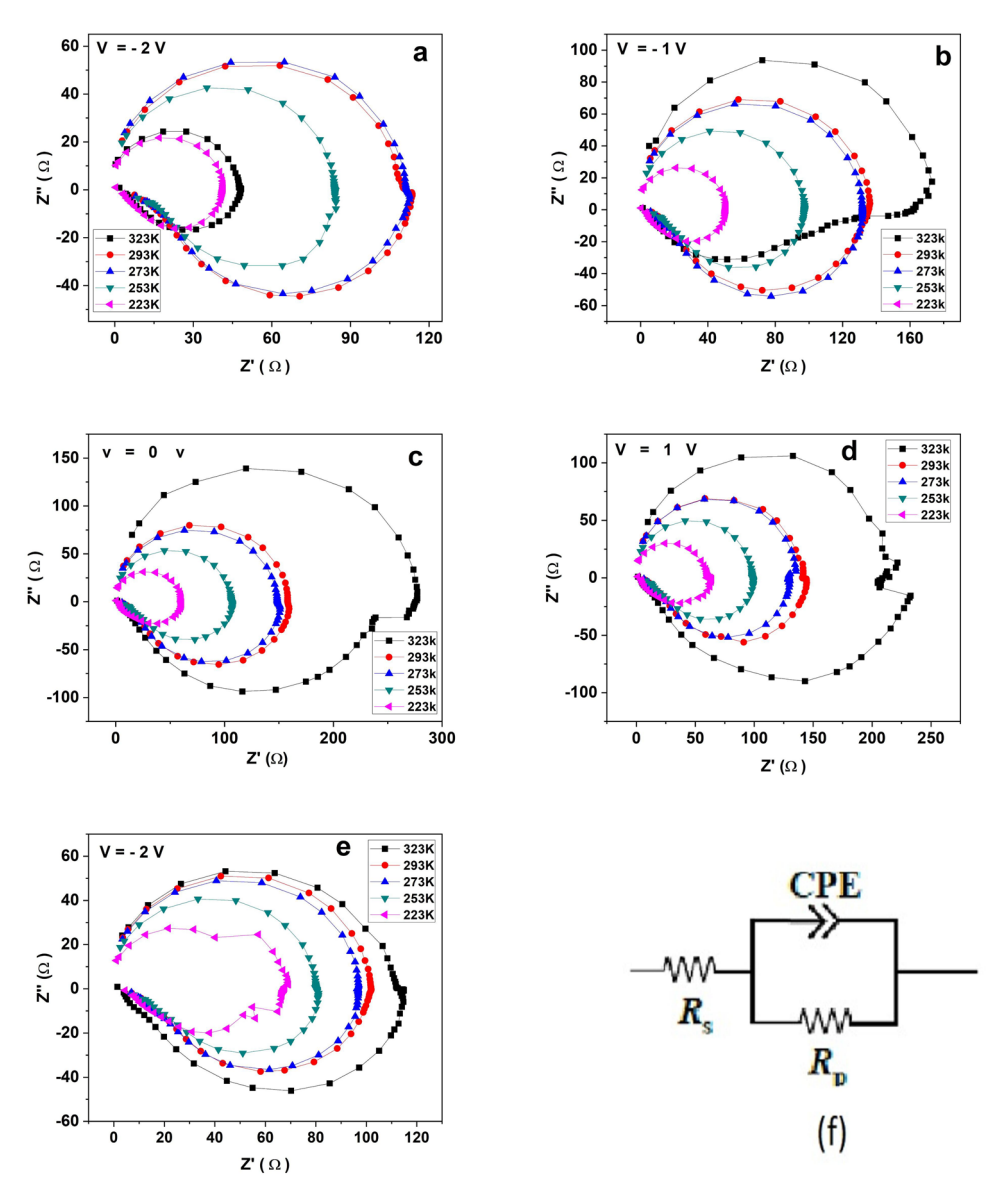


Figure 7: (a)-(e) Col-Col diagram of Z" vs Z' at different temperatures and voltages of Au/PPy-MWCNTs/TiO₂/Al₂O₃/p-Si/Al.

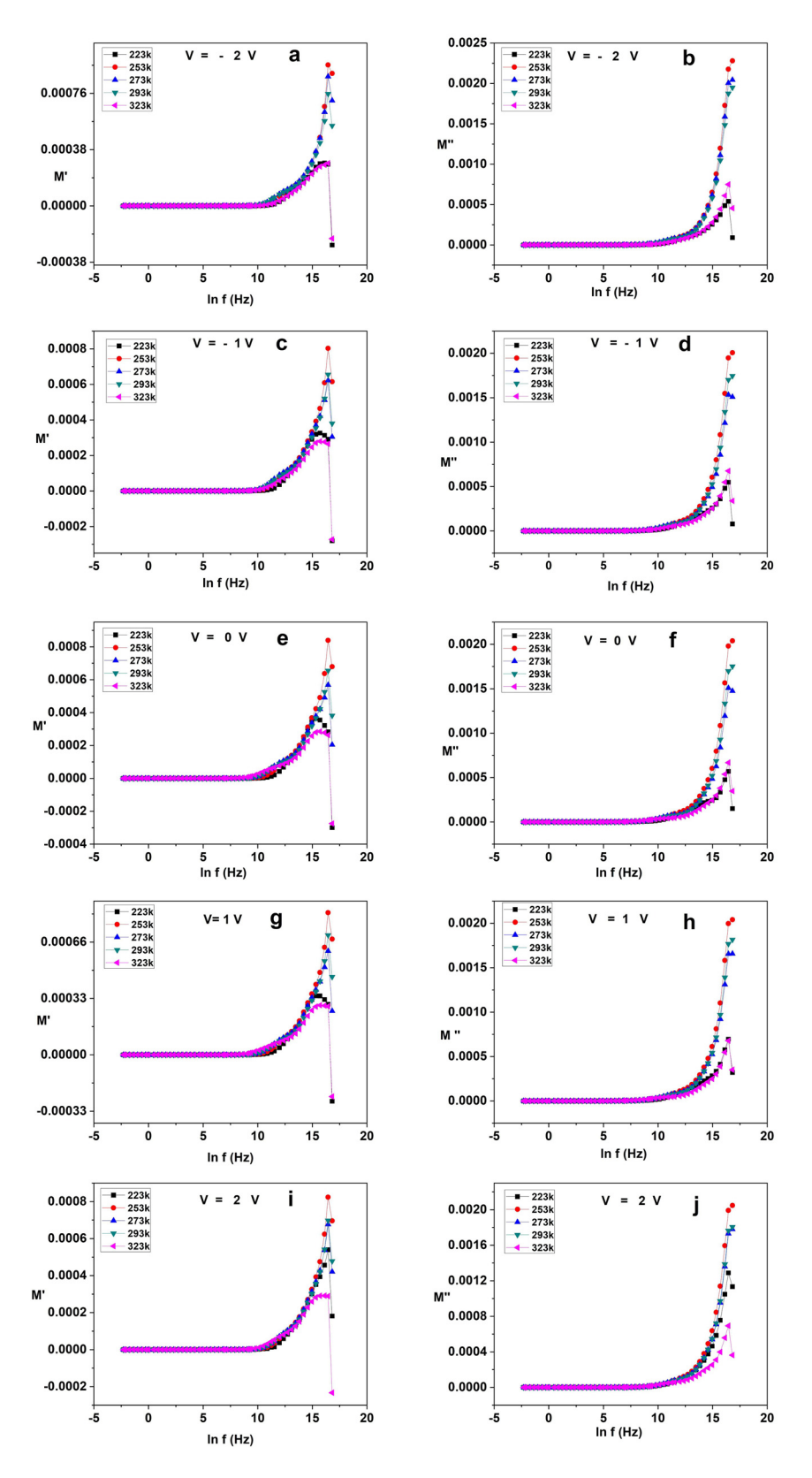
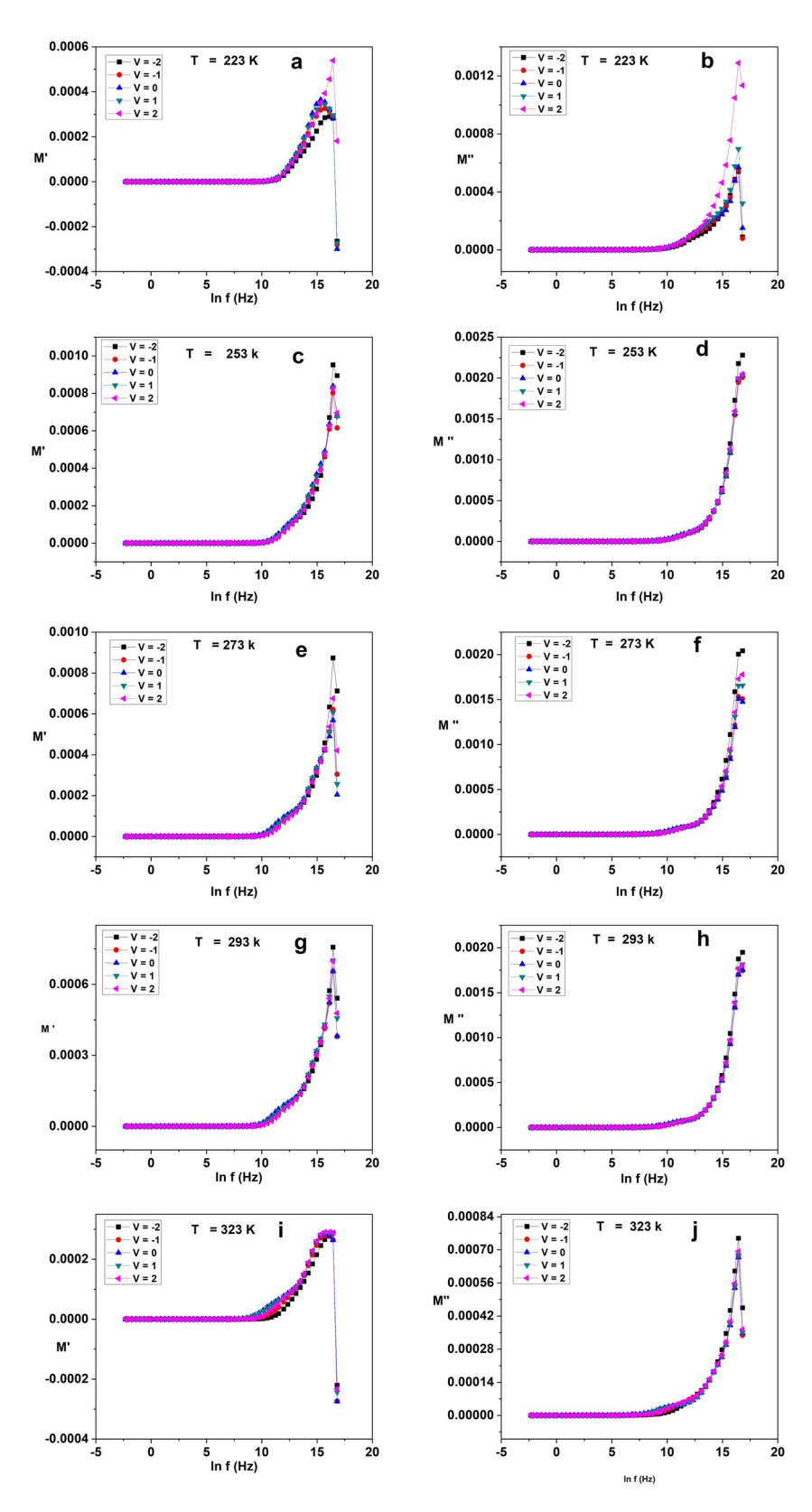


Figure 8: (a)–(j) Frequency dependence of real and imaginary parts of modulus M', M" at different temperatures and voltages of Au/ppY-MWCNTs/ $TiO_2/Al_2O_3/p-Si/Al$.

10 — Adel Ashery et al.



 $\textbf{Figure 9: (a)-(j)} \ \textit{M'}, \textit{M''} \ \textit{vs} \ \textit{lnf} \ \textit{at different voltages and temperatures of } \ \textit{Au/ppY-MWCNTs/TiO}_2/\textit{Al}_2O_3/p-Si/\textit{Al}.$

[31,33,34]. The polarization phenomena related to temperature are discussed by establishing a temperature Cole-Cole diagram based on the dielectric temperature spectrum. The negative value of the electrical conductivity indicates that the electric current flows in the opposite direction to the applied electric field and the associated electrical force. Accordingly, the polarization phenomena related to temperature variations are analyzed by constructing a temperature Cole-Cole diagram derived from the dielectric temperature spectrum. Traditionally, the Cole-Cole diagram is employed to investigate dielectric polarization behavior by examining the frequency dependence of real (€') and imaginary (€") permittivity components at a fixed temperature. In this study, the Cole-Cole equation is modified by incorporating microscopic parameters that characterize the temperature dependence of dielectric polarization, thereby enabling the development of a temperature Cole-Cole diagram. This approach facilitates the investigation of polarization and loss mechanisms based on the dielectric temperature spectrum. The findings of this work offer new insights into the underlying mechanisms governing dielectric polarization and energy dissipation.

Figure 8(a)–(j) illustrates the frequency dependence of the real and imaginary parts of the modulus, M' and M'', at various temperatures and voltages for the Au/ppY-Au/PPy-MWCNTs/TiO₂/Al₂O₃/p-Si/Al structure. As shown in Figure 8(a), (c), (e), (g) and (i), the M' behavior at low and mid frequencies remains unchanged across all temperatures. However, at high frequencies, M' increases, forming peaks with positive values, except for the curves at 323 and 223 K, where the peaks exhibit both positive and negative values at voltages V = -2, -1, 0, 1 V. As shown in Figure 8(b), (d), (f), (h), and (j), at V = 2V, all curves of M' remain positive, except for the curve at 323 K, which shows both positive and negative values. The behavior of M" remains constant across all frequencies except at high frequencies, where it increases significantly. At temperatures of 223 and 323 K, M" forms peaks. The observed dispersion could be attributed to the conduction mechanism, which is influenced by the limited mobility of charge carriers within a small range [35-37].

Figure 9(a)–(j) illustrates the frequency dependence of M and M" under various voltages and temperatures for the Au/ppY-MWCNTs/TiO₂/Al₂O₃/p-Si/Al structure. As shown in Figure 9(a)–(e), M' remains independent of voltage and frequency at low and mid frequencies. However, at high frequencies, M' exhibits dispersion, forming peaks across all voltage levels. For most curves, M shows positive and negative values, except V = 2 V, which only has positive values, as seen in Figure 9(a) at T = 223 K. In Figure 7(b)–(d), M' generates peaks with positive values only. In

contrast, in Figure 9(e) at T=323 K, M reverts to exhibiting both positive and negative values, similar to the behavior shown in Figure 9(a) at T=223 K. Conversely, at low frequencies, both M and M" values approach zero. These findings align with similar results reported in the literature [38,39]. Such variations in the electric modulus behavior can be attributed to dielectric relaxation mechanisms being more sensitive to frequency than to the applied voltage.

Figure 10 illustrates the barrier height ($\Phi_{\rm ap}$) as a function of q/2kT, as described by equation (4) for the Au/PPy-MWCNTs/TiO₂/Al₂O₃/p-Si/Al structure. The plot exhibits a distinct linear region from which the values of $\phi_{\rm ap}$ and $\sigma_{\rm s0}$ can be determined from the intercept on the ϕ_{b0} – axis while $\sigma_{\rm s0}$ is derived from the slope of the linear segment. For the given structure, the intercept and slope correspond to $\phi_{\rm ap}$ = 1.382 eV and $\sigma_{\rm s0}$ = 0.0388 eV, respectively

$$\phi_{\rm ap} = \phi_{b0}(T=0) - \frac{q\sigma_{s0}}{2kT}.$$
 (4)

As shown in Figure 11, the $(n_{\rm ap}^{-1}-1)$ against q/2kT plot, described by equation (5), exhibits distinct characteristics in the low- and high-temperature regions due to the DG distribution of barrier heights at the M/S interface. Consequently, the values $\rho 2$ and $\rho 3$ are determined from the intercepts and slopes in the respective regions of the experimental $(n_{\rm ap}^{-1}-1)$ against q/2kT plots, as depicted in Figure 11. These values are calculated to be -0.456, -0.590, -0.0222, and -0.0130, respectively.

$$\left(\frac{1}{n_{\rm ap}} - 1\right) = \rho_2 + \frac{q\rho_3}{2kT}.\tag{5}$$

Based on the experimental results, both inhomogeneities and potential barrier height variations significantly influence the forward-bias *I–V* characteristics, particularly

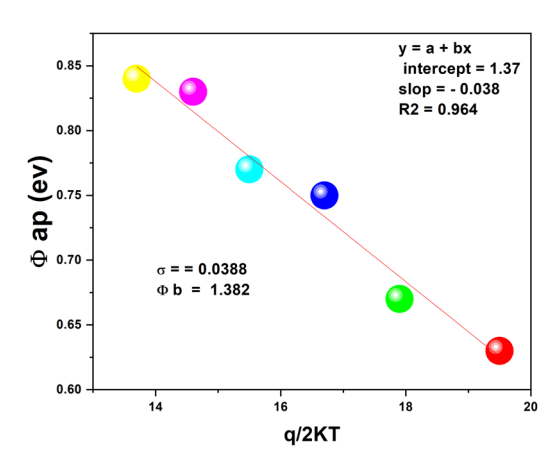


Figure 10: Barrier height vs q/2KT of Au/PPy-MWCNTs/TiO₂/Al₂O₃/p-Si/Al.

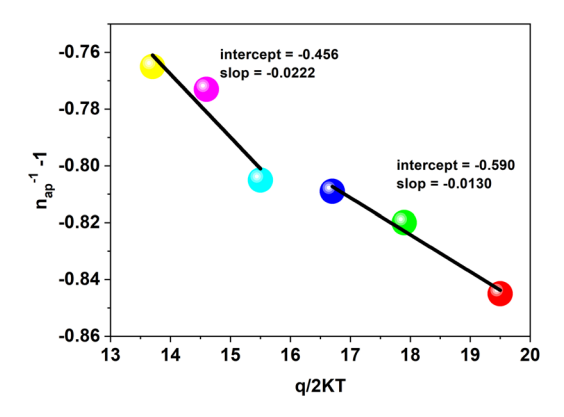


Figure 11: n^{-1} -1 vs q/2KT of Au/PPy-MWCNTs/TiO₂/Al₂O₃/p-Si/Al.

at low temperatures. As a result, the classical Richardson/ Arrhenius model can be refined by combining equations (6) and (7) into the following expression:

$$I = AA^*T^2 \exp\left(\frac{-q\varphi_{B0}}{kT}\right) \left[\exp\frac{q(V - IR_s)}{nkT} - 1\right], \qquad (6)$$

$$\varphi_{B0} = \frac{kT}{q} \ln \left[\frac{AA^*T^2}{I_0} \right]. \tag{7}$$

The modified Richardson plot according to equation (8) for the Au/PPy-MWCNTs/TiO₂/Al₂O₃/p-Si/Al structure is depicted in Figure 12. From the slope and intercept of this plot, the mean barrier height φ_{B0} and the effective Richardson constant (A^*) were determined. These values were found to be 0.99 eV and 50 A cm⁻² K⁻², respectively

$$\ln\left[\frac{I_0}{T^2}\right] - \frac{q^2\sigma^2}{2k^2T^2} = \ln(AA^*) - \frac{q\varphi_{B0}}{kT}.$$
 (8)

Figures 13 and 14 show the plots of $\ln(I_0/T^2)$ against 1/nT and 1/T for the structure. As seen in Figure 13, the plot of \ln

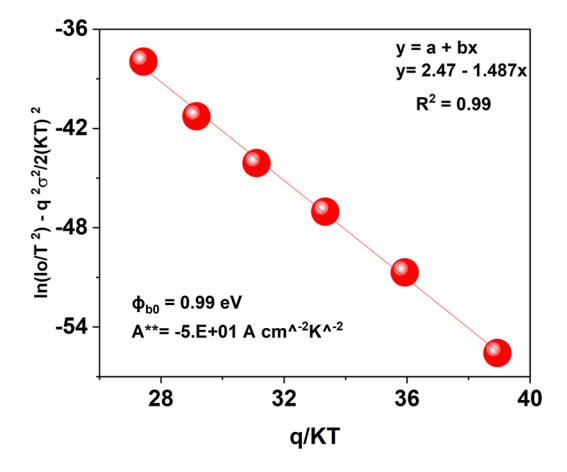


Figure 12: The modified Richardson figures. $ln(I_o/T^2) - q^2 \sigma 2/2(KT)^2 vs q/KT of Au/PPy-MWCNTs/TiO₂/Al₂O₃/p-Si/Al.$

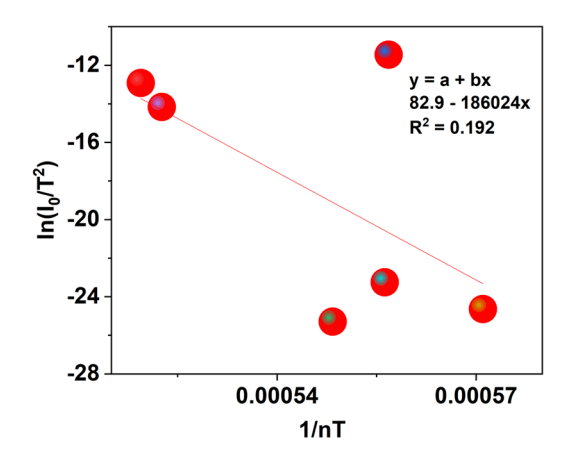


Figure 13: $ln(I_0/T^2)$ vs 1/nT of Au/PPy-MWCNTs/TiO₂/Al₂O₃/p-Si/Al.

 (I_0/T^2) against 1/(nT) is more linear compared to $\ln(I_0/T^2)$ versus 1/T in the measured temperature range. The temperature dependence of the ideality factor and barrier height explains the typical $\ln(I_0/T^2)$ behavior against 1/T. Similar results have been observed by several authors [40].

Figure 15 illustrates the relationship between barrier height and the ideality factor, as described in equation (9), based on the experimental data. The figure shows that the intercept on the barrier height axis can determine homogeneous barrier heights. Within the linear region, the barrier height is calculated to be 1.17 eV. These findings indicate that the current conduction mechanism aligns with the thermionic emission theory [40–42]

$$\varphi_{\rm eff} = \varphi_{\rm R0} - 1.5(n-1)V_{\rm bb}.$$
 (9)

Figure 16 shows the current (I) versus voltage (V) characteristics of the Au/PPy-MWCNTs/TiO₂/Al₂O₃/p-Si/Al structure under dark and illuminated conditions. The current increases across all voltages compared to the dark condition, especially in the forward bias region. This increase in

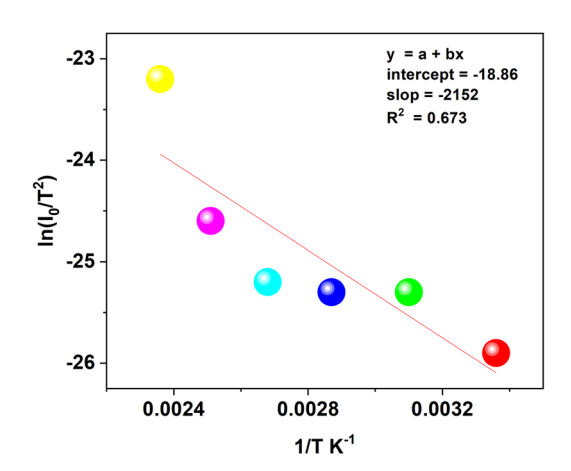


Figure 14: ln(Io/T2) vs 1/T of Au/PPy-MWCNTs/TiO2/Al2O3/p-Si/Al.

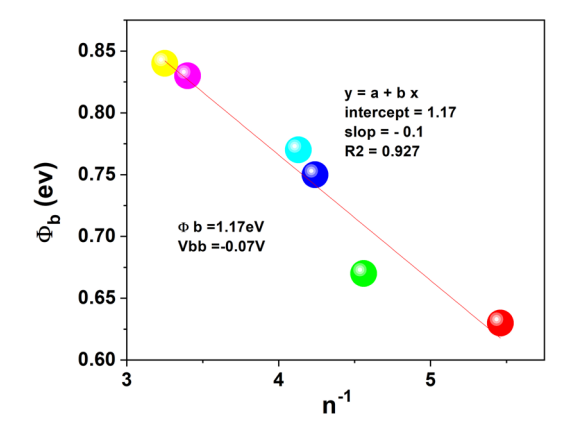


Figure 15: ϕ_b vs n^{-1} of Au/PPy-MWCNTs/TiO₂/Al₂O₃/p-Si/Al.

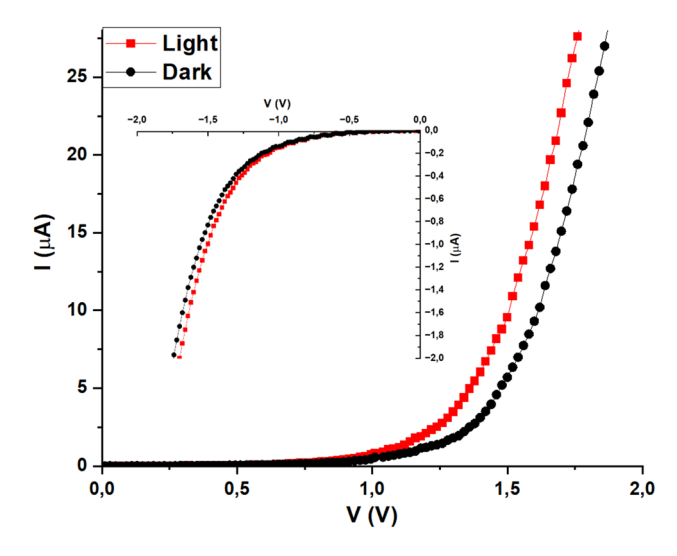


Figure 16: I vs V under the dark and light conditions of Au/ppY-MWCNTs/ $TiO_2/Al_2O_3/p$ -Si/Al. The inset shows the negative bias photocurrent.

current under light exposure demonstrates the structure's ability to generate photocurrent, confirming its functionality as a photodiode. The photocurrent increases from approximately 0.038 A in the dark to 0.052 A under illumination in the forward bias region, indicating enhanced carrier generation due to light absorption. This behavior highlights the structure's potential application in photodetection and optoelectronic devices.

3 Conclusion

The novel structure of Au/PPy-MWCNTs/TiO₂/Al₂O₃/p-Si/Al was synthesized, and its electrical properties were investigated. This structure produces supercapacitors, diodes, sensors, and microelectronic devices. The real part of AC

conductivity at all voltages and temperatures appeared in the low- and mid-frequency ranges but showed a significant increase at higher frequencies. The imaginary part of AC conductivity displayed three behaviors: at low frequencies, its values were positive, while at high frequencies, both negative and positive values were observed. Additionally, at specific temperatures like 293, 273, and 253 K, σ'_{ac} showed only negative values at high frequencies. The real part of impedance (Z') increased with temperature, reaching its maximum at 0 V, but decreased as the voltage increased in both positive and negative regions. The imaginary part of impedance (Z'') exhibited peaks with positive values at low frequencies, while at high frequencies, it showed peaks with negative values. In Cole-Cole diagrams, the semicircles were highly symmetrical and grew with increasing temperature across all voltages, except at V = -2V. The real part of the electric modulus (M) showed positive and negative values; however, at specific temperatures like 253, 273, and 293 K, M' had only positive values. The imaginary part of the modulus (M'') consistently exhibited positive values. The conduction mechanism of the Au/PPy-MWCNTs/TiO₂/Al₂O₃/p-Si/Al structure was also studied.

Funding information: The authors state no funding involved.

Author contributions: All authors have accepted responsibility for the entire content of this manuscript and approved its submission.

Conflict of interest: The authors state no conflict of interest.

Data availability statement: The datasets generated and/ or analyzed during the current study are available from the corresponding author on reasonable request.

References

- [1] Zidan HM, Abdelrazek EM, Abdelghany AM, Tarabiah AE. Characterization and some physical studies of PVA/PVP filled with MWCNTs. J Mater Res Technol. 2019;8(1):904–13.
- [2] Sharika T, Abraham J, George SC, Kalarikkal N, Thomas S. Excellent electromagnetic shield derived from MWCNT reinforced NR/PP blend nanocomposites with tailored microstructural properties. Compos Part B: Enq. 2019;173:106798.
- [3] El Nemr A, Serag E, El-Maghraby A, Fathy SA, Abdel Hamid FF. Manufacturing of pH sensitive PVA/PVP/MWCNT and PVA/PEG/ MWCNT nanocomposites: an approach for significant drug release. J Macromol Sci, Part A:Pure Appl Chem. 2019;56(8):781–93.

- [4] Chaudhary A, Kumari S, Kumar R, Teotia S, Singh BP, Singh AP, et al. Lightweight and easily foldable MCMB-MWCNTs composite paper with exceptional electromagnetic interference shielding. ACS Appl Mater Interfaces. 2016;8(16):10600–8.
- [5] Ramazanov M, Shirinova H, Hajiyeva F, Bychanok D. New polymeric three-phase nanocomposites based on polyvinylidene fluoride, magnetite nanoparticles and multi-walled carbon nanotubes: production, structure and properties. J Inorg Organomet Polym Mater. 2020;30:4783–91.
- [6] Zhu J, Li Q, Che Y, Liu X, Dong C, Chen X, et al. Effect of Na₂CO₃ on the microstructure and macroscopic properties and mechanism analysis of PVA/CMC composite film. Polymers. 2020;12(2):453.
- [7] Ponnamma D, Cabibihan J-J, Rajan M, Pethaiah SS, Deshmukh K, Gogoi JP, et al. Synthesis, optimization and applications of ZnO/ polymer nanocomposites. Mater Sci Eng, C. 2019;98:1210–40.
- [8] Ali F, Kershi R. Synthesis and characterization of La3 + ions incorporated (PVA/PVP) polymer composite films for optoelectronics devices. J Mater Sci:Mater Electron. 2020;31(3):2557–66.
- [9] Mohammed M. Controlling the optical properties and analyzing mechanical, dielectric characteristics of MgO doped (PVA–PVP) blend by altering the doping content for multifunctional microelectronic devices. Opt Mater. 2022;133:112916.
- [10] Arefian M, Hojjati M, Tajzad I, Mokhtarzade A, Mazhar M, Jamavari A. A review of Polyvinyl alcohol/Carboxymethyl cellulose (PVA/CMC) composites for various applications. J Compos Compd. 2020;2(3):69–76.
- [11] Miao J, Zhang R, Bai R. Poly (vinyl alcohol)/carboxymethyl cellulose sodium blend composite nanofiltration membranes developed via interfacial polymerization. J Membr Sci. 2015;493:654–63.
- [12] Hashim A, Hadi Q. Structural, electrical and optical properties of (biopolymer blend/titanium carbide) nanocomposites for low cost humidity sensors. J Mater Sci: Mater Electron. 2018;29:11598–604.
- [13] Hashim A, Hadi Q. Synthesis of novel (polymer blend-ceramics) nanocomposites: structural, optical and electrical properties for humidity sensors. J Inorg Organomet Polym Mater. 2018;28:1394–401.
- [14] Darbasizadeh B, Fatahi Y, Feyzi-Barnaji B, Arabi M,
 Motasadizadeh H, Farhadnejad H, et al. Crosslinked-polyvinyl
 alcohol-carboxymethyl cellulose/ZnO nanocomposite fibrous mats
 containing erythromycin (PVA-CMC/ZnO-EM): Fabrication,
 characterization and in-vitro release and anti-bacterial properties.
 Int J Biol Macromol. 2019;141:1137–46.
- [15] Dhandapani E, Suganthi S, Vignesh S, Dhanalakshmi M, Kalyana Sundar J, Raj V. Fabrication and physicochemical assessment of L-Histidine cross-linked PVA/CMC bio-composite membranes for antibacterial and food-packaging applications. Mater Technol. 2022;37(2):124–34.
- [16] Gahlout P, Choudhary V. EMI shielding response of polypyrrole-MWCNT/polyurethane composites. Synth Met. 2020;266:116414.
- [17] Bhavsar V, Tripathi D. Low and high frequency shielding effectiveness of PVC-PPy films. Polym Bull. 2018;75:2085–104.
- [18] Bhavsar V, Tripathi D. Study of attenuation of microwaves by PPy-Doped PVC films. Polym Eng Sci. 2017;57(1):89–94.
- [19] Gounder Thangamani J, Deshmukh K, Sadasivuni KK, Ponnamma D, Goutham S, Venkateswara Rao K, et al. White graphene reinforced polypyrrole and poly (vinyl alcohol) blend nanocomposites as chemiresistive sensors for room temperature detection of liquid petroleum gases. Microchim Acta. 2017;184:3977–87.

- [20] Das M, Sarkar D. Development of room temperature ethanol sensor from polypyrrole (PPy) embedded in polyvinyl alcohol (PVA) matrix. Polym Bull. 2018;75:3109–25.
- [21] Jonscher AK. The 'universal'dielectric response. Nature. 1977;267(5613):673–9.
- [22] Yıldız D, Altındal Ş, Kanbur H. Gaussian distribution of inhomogeneous barrier height in Al/SiO2/p-Si Schottky diodes. J Appl Phys. 2008;103(12):12.
- [23] Şafak-Asar Y, Asar T, Altındal Ş, Özçelik S. Investigation of dielectric relaxation and ac electrical conductivity using impedance spectroscopy method in (AuZn)/TiO2/p-GaAs (110) schottky barrier diodes. J Alloy Compd. 2015;628:442–9.
- [24] Hoque MM, Dutta A, Kumar S, Sinha TP. Dielectric relaxation and conductivity of Ba (Mg1/3Ta2/3) O3 and Ba (Zn1/3Ta2/3) O3. J Mater Sci Technol. 2014;30(4):311–20.
- [25] Yahia I, Hegab N, Shakra A, Al-Ribaty A. Conduction mechanism and the dielectric relaxation process of a-Se75Te25– xGax (x = 0, 5, 10 and 15 at wt%) chalcogenide glasses. Phys B: Condens Matter. 2012;407(13):2476–85.
- [26] Sindhu S, Anantharaman M, Thampi BP, Malini K, Kurian P. Evaluation of ac conductivity of rubber ferrite composites from dielectric measurements. Bull Mater Sci. 2002;25:599–607.
- [27] Fleig J, Maier J. The polarization of mixed conducting SOFC cathodes: Effects of surface reaction coefficient, ionic conductivity and geometry. J Eur Ceram Soc. 2004;24(6):1343–7.
- [28] Maier J. Defect chemistry and ion transport in nanostructured materials: Part II. Aspects of nanoionics. Solid State Ion. 2003;157(1–4):327–34.
- [29] Varalaxmi N. Impedance Spectroscopic Studies of NiMgCuZn Ferrites. J Mater Sci Eng. 2019;8:527.
- [30] Friesen G, Özsar M, Dunlop E. Impedance model for CdTe solar cells exhibiting constant phase element behaviour. Thin Solid Films. 2000;361:303–8.
- [31] Arredondo B, Martín-López MB, Romero B, Vergaz R, Romero-Gomez P, Martorell J. Monitoring degradation mechanisms in PTB7: PC71BM photovoltaic cells by means of impedance spectroscopy. Sol Energy Mater Sol Cell. 2016;144:422–8.
- [32] Ebrahim S. Impedance spectroscopy and equivalent circuits of heterojunction solar cell based on n-Si/polyaniline base. Polym Sci Ser A. 2011;53:1217–26.
- [33] Aouniti A, Elmsellem H, Tighadouini S, Elazzouzi M, Radi S, Chetouani A, et al. Schiff's base derived from 2-acetyl thiophene as corrosion inhibitor of steel in acidic medium. J Taibah Univ Sci. 2016;10(5):774–85.
- [34] Zhang Y, Li L, Yuan S, Li G, Zhang W. Electrical properties of the interfaces in bulk heterojunction organic solar cells investigated by electrochemical impedance spectroscopy. Electrochim Acta. 2013;109:221–5.
- [35] Najar MH, Majid K. Investigation of the transport properties of PPy/ [Co (EDTA) NH 3 Cl]· H 2 O nanocomposite prepared by chemical oxidation method. RSC Adv. 2016;6(30):25449–59.
- [36] Hazarika J, Kumar A. Electric modulus based relaxation dynamics and ac conductivity scaling of polypyrrole nanotubes. Synth Met. 2014;198:239–47.
- [37] Ranjan R, Kumar R, Kumar N, Behera B, Choudhary R. Impedance and electric modulus analysis of Sm-modified Pb (Zr0. 55Ti0. 45) 1 – x/4O₃ ceramics. J Alloy Compd. 2011;509(22):6388–94.
- [38] Bidault O, Kchikech GPM, Belkaoumi M, Maglione M. Phys Rev B. 1994;49:7868.

- [39] Prabakar K, Narayandass SK, Mangalaraj D. Dielectric properties of Cd0. 6Zn0. 4Te thin films. Phys Status Solidi (a). 2003;199(3):507-14.
- [40] Ashajyothi S, Reddy VR, Kumar AA. Structural, chemical states, electrical properties and forward transport phenomena of Ti/MnO2/p-InP heterostructure with a transition metal oxide MnO₂ interlayer. Phys B: Condens Matter. 2024;683:415957.
- [41] Nikitina I, Vassilevski K, Horsfall A, Wright N, O'Neill A, Johnson C, et al. Structural pattern formation in titanium-nickel contacts on silicon carbide following high-temperature annealing. Semicond Sci Technol. 2006;21(7):898.
- [42] Pattabi M, Krishnan S, Mathew X. Effect of temperature and electron irradiation on the I-V characteristics of Au/CdTe Schottky diodes. Sol Energy. 2007;81(1):111-6.